# A large area detector for high-energy neutrons

## LAND Collaboration

Th. Blaich [e], Th.W. Elze [d], H. Emling [c], H. Freiesleben [a], K. Grimm [d], W. Henning [c,f],
R. Holzmann [c], G. Ickert [c], J.G. Keller [a], H. Klingler [d], W. Kneissl [a], R. König [a],
R. Kulessa [b], J.V. Kratz [e], D. Lambrecht [e], J.S. Lange [a], Y. Leifels [a], E. Lubkiewicz [b],
M. Proft [e], W. Prokopowicz [b], C. Schütter [d], R. Schmidt [c], H. Spies [d], K. Stelzer [d], J. Stroth [c],
W. Walus [b], E. Wajda [b], H.J. Wollersheim [c], M. Zinser [f] and E. Zude [f]

[a] Institut für Experimentalphysik, Ruhr-Universität Bochum, D-4630 Bochum, Germany
[b] Institute of Physics, Jagiellonian University, PL-30-059 Cracow, Poland
[c] Gesellschaft für Schwerionenforschung, D-6100 Darmstadt, Germany
[d] Institut für Kernphysik, Johann-Wolfgang-Goethe-Universität, D-6000 Frankfurt, Germany
[e] Institut für Kernchemie, Johannes-Gutenberg-Universität, D-6500 Mainz, Germany
[f] Institut für Physik, Johannes-Gutenberg-Universität, D-6500 Mainz, Germany

We present design studies, results of test measurements, and Monte Carlo simulations which served as a basis for the realization of a large area neutron detector (LAND). It has a front area of 2 m × 2 m and a depth of 1 m, and features a multilayer structure of passive converter and active scintillator material. The detector is subdivided in independently operating paddles which allow time-of-flight and position measurement. An energy resolution of $\Delta T_n / T_n = 5.3\%$ for a flight path of 15 m and an overall detection efficiency of $\epsilon \approx 1$ is anticipated for neutrons with $T_n \approx 1$ GeV. The operation of LAND at the SIS facility of GSI is described.

## 1. Introduction

A large area neutron detector (LAND) has been built to study neutrons from near-relativistic heavy-ion collisions at the SIS facility of GSI, Darmstadt. The detector will be mainly used in two areas of nuclear reaction physics, namely in studies of neutron flux from central collisions and its relation to the nuclear equation of state, and in investigations of new collective modes excited in very peripheral collisions in both stable and radioactive nuclei. The primary experimental goals are, in the former case, the precise measurement of neutrons and their correlations with charged particles identified with the 4π-detector [1], and in the latter case, the complete measurement of neutron momenta for reconstruction of the invariant mass of the emitting nucleus which is feasible due to strong kinematical focussing in the case of neutron emission from excited projectiles.

Such experiments impose specific requirements on the properties of the detector. Obviously, good spatial and momentum resolution are crucial for the planned applications. Moreover, the detector must allow to resolve multiple hits up to about six; the prerequisite to reach this goal is, besides sufficient granularity, a very high efficiency of $\epsilon \approx 1$. The built detector has for a front face of 2 m × 2 m and 1 m depth. It features a multilayer structure of passive converter and active scintillator material. The detector is subdivided into 200 independently operating modules and a 40-element charged-particle veto counter. Although LAND has the appearance of a calorimeter and can be used for this purpose, its main function concerns time-of-flight (TOF) measurements with very good position as well as time resolution which will give excellent three-momentum resolution.

In this paper we present design studies, results of pilot experiments as well as Monte Carlo simulations which led to the final design. We also show test results for a substructure of the detector, portray the expected properties of the full-size detector, and describe the operation of LAND.

## 2. Design studies

### 2.1. General considerations

Two basic problems are encountered in the measurement of kinetic energies of very energetic neutrons with high efficiency and very good energy resolution. First, for high efficiency a detector is required with a total thickness of several times the nuclear interaction length which amounts to $\lambda_{int} \approx 80$ cm [2] for very energetic neutrons in typical scintillator materials. The total thickness can be reduced effectively by introducing passive converter material as it is done in various types of calorimeters [3–6]. Resolutions of $\sigma(E)/E = 0.35/\sqrt{E/\text{GeV}}$ have been obtained for pions and protons in a momentum range of 0.3–40 GeV$/c$ applying a uranium/copper fine-sampling calorimeter [5]. For the envisaged experiments we aim at a resolution in the order of 5% for neutrons with kinetic energies $T_n \leq 1$ GeV. It is conjectured that calorimeters for such neutrons can hardly be built with a resolution increased by almost an order of magnitude. Thus, high efficiency and good energy resolution exclude each other in case of calorimetric measurements. Second, high resolution measurements of neutron kinetic energies are feasible by means of the time-of-flight (TOF) method. Generally, organic scintillators are used for this purpose since they allow for good time resolution and, hence, energy resolution, and also, to some extent, for particle discrimination by means of pulse shape analysis. The energy resolution, $\delta T_n/T_n$, is given by

$$\delta T_n/T_n = \gamma(\gamma + 1)\left[(\delta S/S)^2 + (\delta T/T)^2\right]^{1/2},$$

where $\gamma$ is the Lorentz factor, $S$ the measured flight path, $T$ the flight time, $\delta S$ and $\delta T$ the respective resolutions [1].

For infinitely good time resolution ($\delta T = 0$), the energy resolution is limited by the finite detector thickness $\Delta S$, because the position of the neutron interaction can be anywhere within the detector. A flight path, hence, is only measured with a resolution of $\delta S = \Delta S$. Already a detector of 10 cm thickness contributes 4% to the energy resolution for neutrons with $T_n = 1$ GeV and $S = 15$ m. Thus, TOF measurements require rather thin detectors if one is limited to flight paths in this order.

A set of large volume plastic-scintillator detectors for neutrons from high energy heavy-ion collisions has been built by Madey et al. [7] and has been used at the BEVALAC [8]. In order to achieve good time resolution, the scintillator thickness was about 10 cm, resulting in a relatively low efficiency in the order of 10%. A considerably improved detection efficiency can be achieved if a TOF neutron detector is applied which is based on the calorimeter principle, i.e. passive converters are introduced. An adequately thick detector then assures the necessary detection efficiency, and a modular configuration is expected to yield a sufficiently good time resolution.

The experimental area at SIS where LAND is installed allows for flight paths up to 15 m. In order to guarantee the acceptance angle as required by the envisaged experiments, a front area of 2 m × 2 m is then necessary. Because of spatial as well as TOF resolution and of multiple hit capability the whole detector has to be divided into modules. Two possible structures were considered: a "paddle structure" and a "tower structure" where the modules are perpendicular or parallel to the neutron direction of incidence, respectively. At first sight, the latter has obvious advantages: if neutron-induced showers of charged particles are contained within a single tower its front area determines the position resolution as well as the capability to recognize multiple hits. However, there is a severe disadvantage: a tower structure requires light collection by means of thin fluorescent light guides along the tower which cause a drastic loss in light collection efficiency. This was shown for a test setup. Although light was detected at both sides of the light guide, the time resolution obtained was poor and imposed a severe and unacceptable limitation on TOF and position resolution. Thus the tower structure was excluded from further studies.

The paddle structure has the advantage that the scintillator stripes serve as efficient light guides: because of total internal reflection, they focus the scintillation light along the directions perpendicular to the neutron incidence. Position information can be obtained from the time difference between the light pulses arriving at the two paddle ends (see below). Thus, by mounting paddles in layers where consecutive layers are oriented perpendicularly to each other, position information is obtained in a plane perpendicular to the neutron's direction of flight. The paddle thickness corresponding to $\Delta S$ as discussed above has to be chosen in accordance with both the accuracy envisaged for position measurement and that required for TOF measurement.

These considerations defined the basic structure of our detector, but many principal questions and technical details remained to be solved. By means of extensive Monte Carlo simulations and test experiments,

---

[1] Throughout this paper we will quote experimental resolution of a quantity $X$ by its value at full width half maximum (FWHM) $\delta X$, while standard deviations (always calculated as square root of the second central moment) are quoted as $\sigma(X)$, and $\delta X = (8 \ln 2)^{1/2}\sigma(X)$ for normal distributions only.

described below, we studied the feasibility of the concept and optimized the detector components.

## 2.2. Monte Carlo simulations

Prior for us to engage in detailed MC simulations the reliability of available computer codes had to be evaluated. The commonly used codes GEANT/ GHEISHA [9] and HERMES/HETC [10] meet requirements of high-energy particle physics. Their adequacy for describing hadronic interactions induced by neutrons with $T_n \leq 1$ GeV had not been shown so far. In order to establish a data base with which MC simulations could be confronted, we performed a pilot experiment at the SATURNE accelerator facility in Saclay, France. It aimed at the investigation of the development and properties of cascades, and at the determination of the efficiency of neutron detection both in scintillator material alone and in multiple iron/scintillator layers.

A test setup of eight scintillator paddles of 1 cm thickness was irradiated perpendicularly to their front area of 50 cm $\times$ 9 cm with neutrons of kinetic energies of $T_n = 200, 500, 850$ MeV from the SATURNE accelerator. Neutrons were produced by deuteron breakup on $^9$Be. About $10^5$ neutrons/s impinged on a central area of $\approx 2$ cm $\varnothing$. The paddles were mounted one after the other with a distance of 5 cm such as to allow the insertion of iron sheets of various thickness as passive converters. Photomultipliers on either side of the scintillator detected visible energy, i.e. scintillation light. The first scintillator was used as veto counter against charged particles travelling along with the neutron beam. The spatial separation of the paddles facilitated the determination of that particular paddle which "fired" first. With respect to this paddle the firing sequence of other paddles was recorded and the efficiency of the setup was determined.

The efficiencies of the setup for various experimental conditions are compiled in fig. 1. They are plotted against a relative paddle number: positive numbers refer to paddles downstream, negative ones to paddles upstream with respect to that paddle which fired first (relative paddle number 0). The hooklike shape observed for the experimental data (full dots) is readily explained by charged secondary particles (mainly protons) which deeply penetrate in forward direction. The slope is partially due to the decreasing solid angle of consecutive paddles with respect to the position of the first hit. The events at negative relative paddle numbers originate from slow secondary particles moving in backward direction. They are more likely to be reabsorbed, thus yielding a much steeper decline.

Comparison of data at $T_n = 200$ MeV for scintillators without iron (upper left frame) with those where 1 cm iron was inserted in front of all but the veto paddle
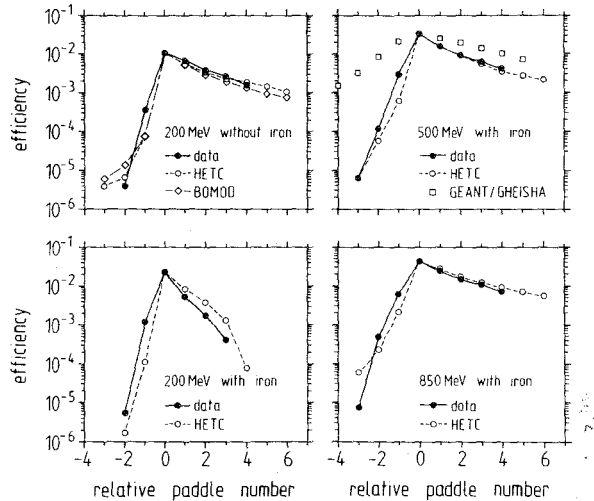


Fig. 1. Efficiencies of the eight-paddle test configuration for various neutron beam energies. The efficiency is plotted with respect to that paddle which fired first (no. 0). The data are compared with results obtained by various Monte Carlo codes. See text for details.

(lower left frame) shows a significant increase of the efficiency by a factor of 2.4 for the first interaction producing visible energy. At the same time reabsorption of charged secondary particles in forward and backward direction is drastically enhanced by the Fe converter. Fig. 1 also contains a comparison with the predictions of various MC codes. Calculations at $T_n = 500$ MeV (upper right frame) show that GEANT/ GHEISHA (version 3.12) yields too large an efficiency while HETC results describe the data very well. This is also observed at $T_n = 850$ MeV (lower right frame). The efficiency of consecutive scintillators represented by the hooklike shapes in fig. 1 depends strongly on the reabsorption of secondary shower particles in the converter material. This process is of less influence with increasing neutron energy. For the case of scintillators without iron we used, in addition, the code BOMOD which is a derivative of the MC code of Stanton et al. [11]. This code is known to reproduce excellently the response of plastic and liquid scintillators to neutrons of $T_n \leq 200$ MeV [12]. Since BOMOD and HETC predictions nicely agree with data at $T_n = 200$ MeV as well as HETC predictions with data at $T_n = 500, 850$ MeV we decided to fully rely on HETC for our design considerations. One should keep in mind that the agreement of data and HETC predictions at low neutron energies, in case of iron converters (lower left frame), is not as good as at higher energies.

Next we investigated, by means of HETC, the efficiency of an iron/scintillator structure of 20 cm depth for monoenergetic neutrons impinging perpendicularly
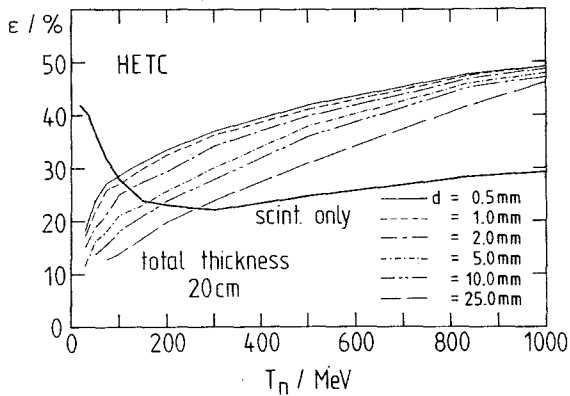
Fig. 2. Calculated efficiencies of an iron/scintillator structure of 2 m × 2 m area and a depth of 20 cm as a function of neutron kinetic energy. Various layer thicknesses $d$ (with $d(\text{Fe}) = d(\text{scint})$) are considered. The thick solid line is for pure scintillator material.



Fig. 3. Experimentally determined absorption lengths (solid dots), in comparison to the interaction length, $\lambda_{int}$, and collision length, $\lambda_{coll}$, of neutrons of $T_n = 800$ MeV in various absorber materials as given in ref. [2].

on the front area of 2 m × 2 m. Various ratios of layer thickness were considered. In fig. 2 the efficiency for producing visible energy in this structure is shown as function of neutron energy, the parameters of the curves are the layer thickness $d$ under the condition that $d(\text{iron}) = d(\text{scintillator})$. A light output threshold of 1 MeV electron equivalent energy was applied in these calculations, but light attenuation along the paddles was not taken into account. It is seen that the efficiency of the structure increases as the layers become thinner. The smallest layer thickness of 0.5 mm is pretty close to a homogeneous mixture of converter and scintillator considering the interaction length $\lambda_{int}$ in either material. Taking into consideration light attenuation, which depends strongly on the scintillator thickness, mechanical stability and, last but not least, financial aspects, we decided on a layer structure with $d = 5$ mm. Calculations performed with lead instead of iron resulted in comparable efficiencies due to the similarity of the interaction lengths in iron and lead. For economical reasons we decided to use iron. The curve labelled "scintillator only" shows that the sandwich structure is superior for $T_n > 150$ MeV.

In the course of the experiment at SATURNE we also determined from a beam transmission experiment the absorption length of neutrons of $T_n = 800$ MeV in various materials. The results are shown in fig. 3. The statistical errors of the data are smaller than the symbol size. The two curves labeled $\lambda_{int}$ and $\lambda_{coll}$ result from mean free paths between collisions ($\lambda_{coll}$) or inelastic interactions ($\lambda_{int}$) of high energy neutrons in polyethylene, concrete, iron, and lead, which are taken from ref. [2]. From $\lambda(\text{Fe}) \approx 113$ g/cm$^2 = \rho \times 14.4$ cm we concluded, that a converter with an overall thickness of 50 cm interspersed by a total of 50 cm scintilla-

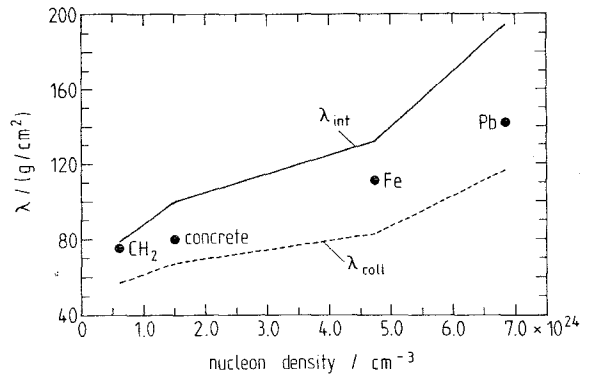tor material, and arranged in consecutive layers of 5 mm thickness, will provide the required efficiency.

### 2.3. The final design

The Monte Carlo studies described in the previous subsection led to the final design described in the following. The full detector sketched in fig. 4 is subdivided into 200 paddles of 200 cm × 10 cm area and 10 cm depth. A single paddle is shown in fig. 5. Each paddle contains 11 sheets of iron (the two outer ones are 2.5 mm thick, the others are 5 mm thick) and 10 sheets of 5 mm thick scintillator, mounted in an iron-sheet box which has a wall thickness of 1 mm. 20 paddles are arranged in one layer; subsequent layers are mounted with the paddles perpendicular to each other, thus giving position information in both vertical
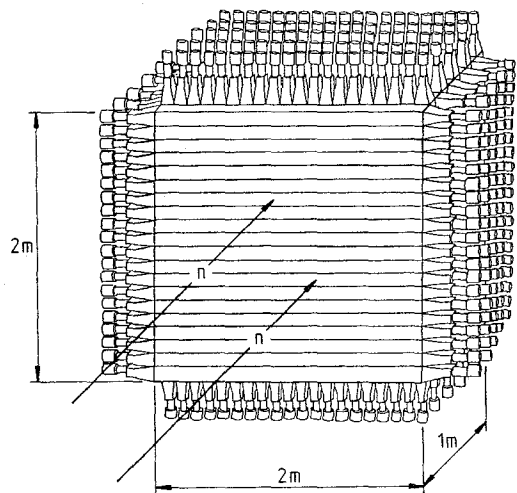


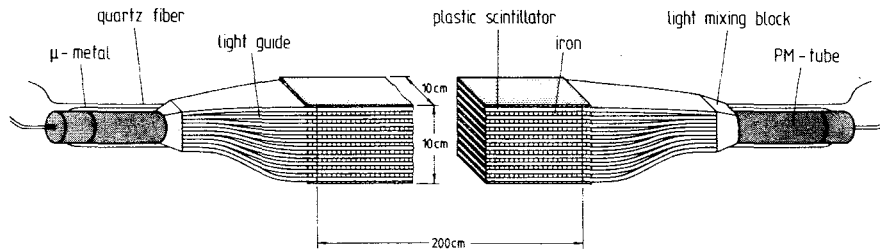Fig. 4. Sketch of the full neutron detector (without veto detector).

Fig. 5. Sketch of one neutron detector paddle. The layer structure is shown together with the bent light guide strips, light mixing blocks, quartz glass fibers, and photomultipliers.

and horizontal directions, orthogonal to the neutron incidence.

Light produced in a paddle is collected by means of stripe light guides (cf. fig. 5) on both ends of the scintillator sheets and is directed to the photomultipliers. The difference in arrival time of the two signals serves to localize the position where scintillation light was produced by secondary, charged particles; the mean time provides TOF information.

In front of LAND a veto detector for charged particles is installed. It consists of two crossed layers, each with 20 scintillators strips. Their size of 200 cm × 10 cm × 0.5 cm matches the neutron paddle size. Again, the light is read out at both ends of each of the 2 × 20 strips in order to obtain position and TOF information.

As a by-product, the veto detector allows for identification of charged particles via $\Delta E$–TOF analysis, Thus we are able to compare directly neutron and charged particle aspects of heavy-ion collisions under identical experimental conditions.

## 2.4. Optimization of detector components

Detailed investigations were carried out to optimize the time response of the paddles. A prototype was exposed to cosmic rays, UV light pulses from a $N_2$-laser with subnanosecond rise time and to minimum ionizing electrons (40 MeV) from the LINAC at the Strahlenzentrum of the University of Giessen. Various plastic scintillator materials, photomultipliers and light guides of different shapes were considered in these tests.

The resolution achieved for the time-of-flight and position measurements crucially depends on both the amount of light produced by secondary charged particles in the scintillator, and on the pulse rise time. Therefore it is indispensable to choose plastic material with a high intrinsic light output, a large light attenuation length and a short light decay time. Among these quantities a compromise had to be found.

We concentrated on plastic scintillators with intrinsic light decay times around 2 ns, with ≈ 60% light output of anthracene, and with a bulk attenuation length of about 4 m. Because of multiple reflections of the light in the 5 mm thin and 2 m long plastic strips the effective light attenuation length, however, deteriorates considerably depending on the quality of the scintillator surface. In table 1 we present the effective attenuation length of various scintillator materials as obtained by feeding, through quartz-glass fibres, UV light of known intensity into well defined positions, and by observing the intensity of the induced scintillation light at both ends of the paddle. The scintillator BC 408 was finally selected; relevant properties of investigated scintillators are listed in table 1.

We also investigated the time resonance of a number of photomultiplier tubes of 2 in. ∅ and 3 in. ∅. Only commercially available photomultipliers within a certain cost limit were considered. Although the 2 in. tubes collect only half the light compared to the 3 in.

Table 1

Measured effective attenuation length $\lambda_{eff}$ of various scintillator material (5 mm thick), together with other parameters as quoted by the manufacturers

| Scintillator | Light output [% anthrazene] | Decay time [ns] | Max. emission wavelength [nm] | H/C ratio | Density [g/cm³] | Refraction index | $\lambda_{eff}$ [cm] |
|---|---|---|---|---|---|---|---|
| NE 102A [a] | 65 | 2.4 | 423 | 1.104 | 1.032 | 1.58 | 120 |
| BC 408 [b] | 64 | 2.1 | 425 | 1.104 | 1.032 | 1.58 | 230 |
| KYOWA SCSN 38 [c] | 60 | 2.5 | 430 | – | – | – | 85 |
| KYOWA SCSN 81 T2B [c] | 60 | – | 435 | – | – | – | 155 |

[a] Provided by Nuclear Enterprise Ltd., Edinburgh, UK.
[b] Provided by Bicron Corporation, 2410 AG Bodegraven, Netherlands.
[c] Provided by Mitsui + Co., Düsseldorf, Germany.

Table 2
TOF resolution obtained from mean-timing using various 12-stage photomultiplier tubes on a prototype paddle; values quoted are FWHM. A 40 MeV electron beam was used. Parameter of the photomultiplier tubes as quoted by the manufacturers are also listed

| Type | TOF resolution FWHM [ps] | Anode pulse rise time [ns] | Quantum efficiency [%] |
|---|---|---|---|
| XP2020 [a] | 260 | 1.5 | 25 |
| R1828-01 [b] | 260 | 1.3 | 25 |
| XP2262 [a] | 290 | 2.0 | 25 |
| XP2282 [a] | | | |
| (8-stage) | 320 | 1.5 | 28 |
| 9821B [c] | 340 | – | – |

[a] Provided by Valvo, Hamburg, Germany.
[b] Provided by Hamamatsu Photonics, Herrsching, Germany.
[c] Provided by THORN EMI Ing.-Büro Dörr, Stuttgart, Germany.

tubes, they showed the better timing characteristic in our application, primarily because of their faster intrinsic pulse rise time (typically $\approx$ 2 ns) as compared to the 3 in. $\varnothing$ tubes (typically > 3 ns). In table 2 we present the TOF resolution measured through mean-timing from two photomultiplier tubes from the same production series. For that purpose we built a prototype paddle as described above, however the iron sheets were removed. The paddle was then exposed to 40 MeV electrons from the LINAC at the Strahlenzentrum of the University Giessen; a thin plastic counter served as trigger for the incident electrons. An electron beam was chosen for this measurement because the energy deposit of electrons is comparable to that of shower particles induced by energetic neutrons. For economical reasons, we finally decided for the XP2262(2 in.) tube. The spectral sensitivity of this phototube peaks at 420 nm and, thus, matches very well the wavelength of maximal emission of the BC 408 scintillator (425 nm). A special passive voltage divider with a total resistance of 2.6 M$\Omega$ was developed for our application (Type 56628, supplied by Valvo, Hamburg, Germany).

Finally we considered different shapes of light guides which collect light from the ten scintillator sheets contained in each paddle. The final version is made out of ten bent strips which merge into a 2 cm long light mixing block. The lengths of the bent strips vary slightly in such a way as to partly compensate for the time-of-flight neutrons need to traverse the paddle. PMMA material, provided by Pol.hi.tech., Carsoli, Italy, is used which shows maximum and nearly constant transmission for light of wavelength $\geq$ 390 nm.

Silicon pads of 2 mm thickness provide the optical link between the three components, scintillator, light guide, and photomultiplier tube. The silicon pads were prepared following the prescriptions given in ref. [13]. According to this work, the long term behaviour is satisfactory, in particular in an environment with high radiation level. The silicon pads also serve as a mechanical buffer between scintillator and light guide strips, where small mechanical tolerances need to be compensated. The transmission through the silicon pads was measured to be $\approx$ 92% for light with wavelengths $\geq$ 360 nm [14].

## 3. Properties and performances of LAND

### 3.1. Results of test experiments with prototype paddles

The characteristics of arbitrarily selected paddles of the structure described above were determined experimentally. The linearity of the position response was obtained using cosmic rays, their direction of incidence was defined by two small plastic trigger counters on opposite sides of the paddle; the result is shown in fig. 6. The deviation $\Delta_{pos}$ of the position, calculated from the timing signals from the two photomultipliers, from the true position amounts to less than 1 cm and does not show any systematic shift along the paddle. Hence, the position of light production can easily be determined from the signal arrival time without any correction. In these measurements we observed that 200–300 photoelectrons were produced by the photocathode in case of a cosmic ray particle traversing the center of the paddle. It should be mentioned that cosmic rays produce a light output which is comparable to that of neutron induced shower particles. A similar measurement was performed for the 5 mm thin plastic strips forming the charged-particle veto counter. In this case we observed about 50 photoelectrons. The effective light attenuation lengths were determined in the same test experiment. An average value of $\lambda$ = 240 cm was obtained for 14 paddles.
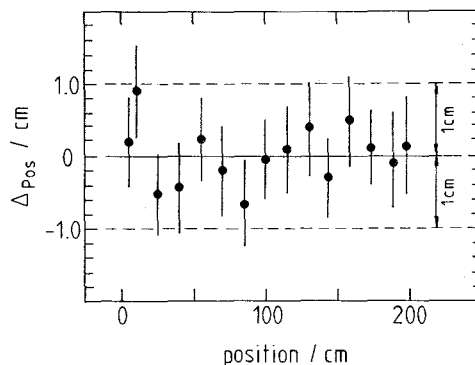


Fig. 6. Deviation of the measured position of light production from the real position for an arbitrarily selected neutron detector paddle. Cosmic radiation was used for this measurement.

During the setup phase of LAND a calibration scheme was developed utilizing cosmic radiation. Details of these procedure will be outlined in section 4.3. It yields, as a by-product, the light attenuation lengths of the paddles. These results are shown in fig. 7 for $\approx 120$ paddles. Practically all fulfil the requirement of $\lambda > 200$ cm; the scatter in $\lambda$ is of no importance for the present purpose.

Further investigations were carried out with tagged neutrons obtained via elastic scattering on protons utilizing the neutron beam of the SATURNE accelerator at Saclay. The experimental setup is displayed in fig. 8. Neutrons were scattered on a $(CH_2)_n$ target and, for comparison, on a carbon target. A beam monitor served for normalization of data taken on the two targets. Pions and $\alpha$-particles were discriminated against recoiling protons from n–p scattering as well as those produced by quasi-free scattering on carbon via energy loss $(dE/dx)$ in the two scintillators $P_1$ and $P_2$. The sizes of the scintillator paddles were 50 cm $\times$ 9 cm $\times$ 1 cm and 50 cm $\times$ 5 cm $\times$ 5 cm, respectively, with the 50 cm length placed symmetrically along the $Z$-axis (cf. fig. 8 for coordinate system). Timing signals from photomultipliers on either end of both paddles were used to determine the position of incidence, and, via mean-timing, to measure the TOF with respect to the start detector (10 mm thick plastic scintillator).

The start detector was also used to initiate the TOF measurement for neutrons. They were detected in an array of ten neutron paddles. The paddles were mounted with their length of 2 m along the $Z$-direction symmetrically with respect to the horizontal plane. The veto detector no. 2 ($V_2$) served to reject charged particles produced in the target and moving towards the neutron detector (N). Veto detector no. 1 ($V_1$) rejected charged particles travelling along with the neutron beam. A tagged neutron is then defined by the trigger condition $\overline{V}_1 \cap \overline{V}_2 \cap S \cap P_1 \cap P_2 \cap N$ where anyone of the ten neutron paddles may have fired. The neutron beam energy was $T_{n\text{-beam}} = 250$, 600 and 1000 MeV.
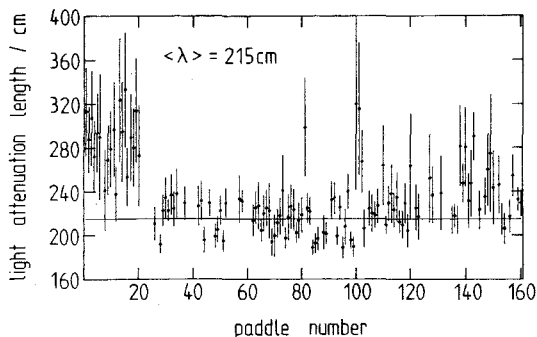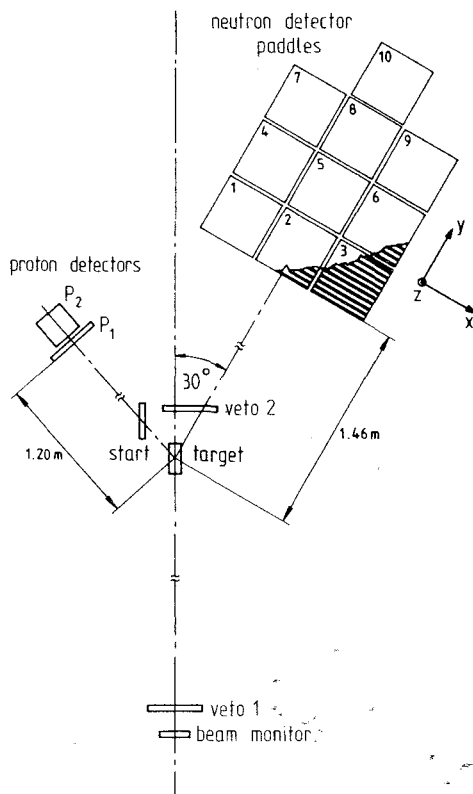


Fig. 8. Setup of a test experiment with tagged neutrons for ten neutron detector paddles. $P_1$, $P_2$: proton paddles; the coordinate system referring to the neutron paddles is indicated. All detector elements but the two distances are drawn on the same scale.

The neutron detector was kept at $\Theta_n = 30°$ while the proton paddles were set according to two-body kinematics at $\Theta_p = 56.7$, 52.7 and 48.5°, respectively. The kinetic energies of the neutrons impinging on the neutron detector were then $T_n = 181$, 417 and 662 MeV, respectively. Since the laser calibration system was not fully operational during this test experiment, it served only for a relative time calibration; the absolute time calibration of the whole setup was performed by utilizing the data obtained for n–p elastic scattering.

The efficiency of the neutron paddle array was determined as the ratio of the proton–neutron coincidence rate to the free proton rate on the $(CH_2)_n$ target taking into account the corresponding rates measured with the C target. The results are displayed in fig. 9. The error bars reflect the statistical uncertainties. The dashed line is the result of a HETC calculation for the neutron paddle array used in the SATURNE experiment. For these calculations, we have used a light output threshold of $L_{thr} = 1$ MeV electron equivalent energy, which corresponds roughly to the setting of the constant fraction discriminators in the timing circuit.



Fig. 7. Effective light attenuation lengths, $\lambda$, of $\approx 120$ neutron detector paddles. $\lambda$ was determined in the course of a calibration of LAND with cosmic radiation (cf. section 4.3).
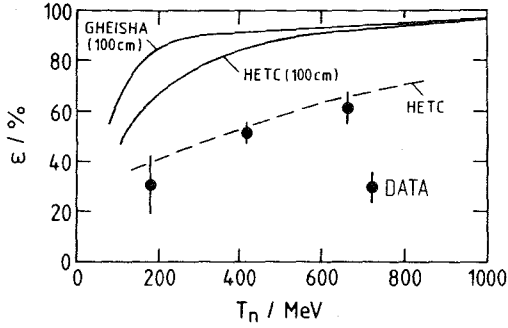
Fig. 9. Measured efficiency of the test setup for tagged neutrons of $T_n = 181$, 417 and 662 MeV. The dashed curve is the result of a Monte Carlo simulation using the HERMES/HETC code for the same geometry. The efficiency of the full size detector (100 cm thick) is also shown as predicted by GEANT/GHEISHA and HERMES/HETC.

However, the efficiency is not too sensitive to $L_{thr}$ since, at least for high-energy neutrons, much light is produced by charged secondary particles. The data are rather well reproduced by the simulation within the experimental errors. There is a tendency, in particular at the lowest neutron energy, of overestimating the efficiency which was already mentioned when discussing the predictions of MC codes in the context of fig. 1. For comparison we also included the efficiency for the full-size detector of 1 m depth, as predicted by HETC and GEANT/GHEISHA. According to HETC simulations the detector will have an efficiency $\epsilon > 90\%$ for neutrons with $T_n > 550$ MeV.

A TOF spectrum for tagged neutrons of $T_n = 417$ MeV from a 600 MeV neutron beam is displayed in fig. 10. The upper frame shows the results obtained for the $(CH_2)_n$ target, the middle frame that for the C target, and the lower frame the difference of the two properly normalized spectra. These spectra were accumulated under the software condition that the protons hit the second paddle $P_2$ within a vertical position of $\Delta Z = \pm 2.5$ cm and that light production occurred only in neutron paddle no. 2 (cf. fig. 8). In that case it is very likely that we also deal with neutrons which had their first interaction in paddle no. 2. The measured time resolution of $\delta T \approx 670$ ps can fully be explained by various uncertainties introduced through the experi-
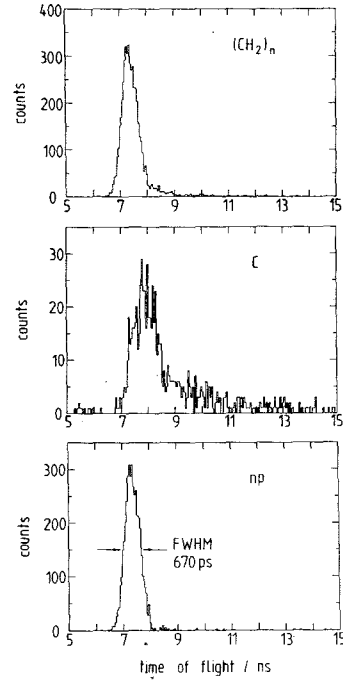


Fig. 10. Time-of-flight spectrum of tagged neutrons of $T_n = 417$ MeV. Upper frame: $(CH_2)_n$-target; middle frame: C-target; lower frame: difference spectrum obtained after proper normalization of the spectra shown in the two frames above.

mental setup, as verified by extensive MC simulations. The numerical values of these uncertainties (FWHM) are listed in table 3 for the three neutron energies. They are due to the following effects:

1) The uncertainty in the position of the neutron interaction in the comparatively large target results in an angular spread of the emitted neutrons of $26.3° \le \Theta_n \le 34.2°$, which introduces a time uncertainty of $\delta T_{geom}$ in the neutron TOF, even for monoenergetic neutrons.

2) The primary neutron beam has an intrinsic time spread of $\delta T_{n\text{-}beam}$ due to its production by deuteron breakup on $^9$Be [15].

3) The recoiling protons suffer an energy loss in the target which depends on the effective thickness that the protons have to traverse after their production.

Table 3
Various contributions ($\delta T_{geom}$, $\delta T_{n\text{-}beam}$, $\delta T_{start}$, $\delta T_{PM}$, $\delta T_{trans}$) to the simulated time resolution, $\delta T_{sim}$, in comparison to the experimental value, $\delta T_{exp}$. The deduced intrinsic resolution is $\delta T_{LAND}$ (see text for details). All values are FWHM

| $T_n$ [MeV] | $\delta T_{geom}$ [ps] | $\delta T_{n\text{-}beam}$ [ps] | $\delta T_{start}$ [ps] | $\delta T_{PM}$ [ps] | $\delta T_{trans}$ [ps] | $\delta T_{sim}$ [ps] | $\delta T_{exp}$ [ps] | $\delta T_{LAND}$ [ps] |
|---|---|---|---|---|---|---|---|---|
| 181 | 469 | 259 | 255 | 474 | 306 | 819 | 1150 | 421 |
| 417 | 375 | 100 | 130 | 474 | 231 | 668 | 670 | 370 |
| 662 | 348 | 61 | 101 | 474 | 206 | 634 | 680 | 356 |

This yields, together with the slightly varying flight path to the start detector, an uncertainty in the start time of $\delta T_{\text{start}}$.

4) The time resolution of the two photomultipliers on the neutron paddle was determined separately to be $\delta T_{\text{PM}}^{n} = 410$ ps each, yielding a mean-timing resolution of $\delta T_{\text{mean-timing}} \approx 290$ ps; that of the PM on the start detector was $\delta T_{\text{PM}}^{\text{start}} = 375$ ps. The resulting time resolution solely due to the PM$_{s}$ is then $\delta T_{\text{PM}} = 474$ ps. This value is independent of neutron energy.

5) Due to the paddle thickness of 10 cm the position of light production is uncertain to this value leading to a further time spread of $\delta T_{\text{trans}}$ which depends on the neutron's kinetic energy.

Taking into account Gauss' error propagation law one obtains the overall resolution of $\delta T_{\text{sim}}$ which is to be compared with the experimental value of $\delta T_{\text{exp}}$. The intrinsic time resolution of a paddle is solely determined by the paddle's photomultipliers resulting in $\delta T_{\text{mean-timing}}$ and the time uncertainty $\delta T_{\text{trans}}$. In the application of LAND, a start signal for TOF measurements will be provided by a dedicated detector which has a time spread much less than that used in the present test experiment. The envisaged time resolution of LAND is then expected to be $\delta T_{\text{LAND}} \approx (\delta T_{\text{mean-timing}}^{2} + \delta T_{\text{trans}}^{2})^{1/2}$. TOF measurements with LAND for neutrons of $T_{n} = 1$ GeV and the longest possible flight path of 15 m in the experimental area will thus result in momentum resolution of $\delta p_{n}/p_{n} = 3.6\%$ or kinetic energy resolution of $\delta T_{n}/T_{n} = 5.3\%$.

In fig. 11, we show the position spectrum of neutrons detected in paddle no. 2 (cf. fig. 8), where in the upper frame the results from a $(CH_2)_n$ target and in the middle frame that from a C target are displayed. The lower frame represents the difference of the former two spectra, which were properly normalized prior to subtraction. As in the case of the TOF spectrum, we required the position of proton incidence to be within $\Delta Z = \pm 2.5$ cm around the horizontal plane. Again, various uncertainties contribute to the FWHM of the position spectrum, their values are listed in table 4:

1) The time spread $\delta T_{\text{geom}}$ (see above) transforms into a position spread $\delta Z_{\text{geom}}$ through $\delta Z_{\text{geom}} = \delta T_{\text{geom}} v_{\text{sc}}$ where $v_{\text{sc}}$ is the average propagation velocity of
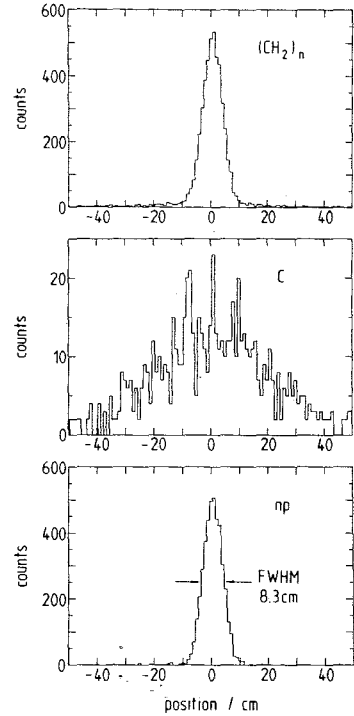


Fig. 11. Neutron position spectrum of $T_{n}^{t} = 417$ MeV. Upper frame: $(CH_2)_n$-target; middle frame: C-target; lower frame: difference spectrum obtained after proper normalization of the spectra shown in the two frames above.

light within the thin scintillator sheets and the connected light guides. The experimentally determined value using laser induced scintillation light (see section 4.3) is $v_{\text{sc}} \approx 15.7 \pm 0.3$ cm/ns.

2) The window on the proton paddle is projected by the corresponding neutrons onto the neutron paddle. This geometrical effect contributes $\delta Z_{\text{proj}}$.

3) Due to the time resolution of the photomultipliers of $\delta T_{\text{PM}}^{n} \approx 410$ ps on the neutron paddles as well as on the proton paddles, the position can only be measured with an accuracy of $\delta Z_{\text{PM}} = \delta T_{\text{PM}} v_{\text{sc}}$.

We obtain with Gauss' error propagation $\delta Z_{\text{sim}}$. The values (FWHM) listed in table 4 agree quite well with the experimental values of $\delta Z_{\text{exp}}$. The intrinsic position resolution of a neutron paddle is exclusively

Table 4
Various contributions ($\delta Z_{\text{geom}}$, $\delta Z_{\text{proj}}$, $\delta Z_{\text{PM}}$) to the simulated position resolution, $\delta Z_{\text{sim}}$, in comparison to the experimental value, $\delta Z_{\text{exp}}$. The deduced intrinsic resolution is $\delta Z_{\text{LAND}}$ (see text for details). All values are FWHM

| $T_{n}$ [MeV] | $\delta Z_{\text{geom}}$ [cm] | $\delta Z_{\text{proj}}$ [cm] | $\delta Z_{\text{PM}}$ [cm] | $\delta Z_{\text{sim}}$ [cm] | $\delta Z_{\text{exp}}$ [cm] | $\delta Z_{\text{LAND}}$ [cm] |
|---|---|---|---|---|---|---|
| 181 | 3.7 | 4.0 | 7.1 | 8.2 | 9.5 | 5.1 |
| 417 | 3.8 | 4.0 | 7.1 | 8.1 | 8.3 | 5.1 |
| 662 | 4.1 | 4.0 | 7.1 | 8.2 | 8.2 | 5.1 |

determined by the time resolution of its photomultipliers and is $\delta Z_{int} = \delta Z_{LAND} \approx 5.1$ cm. This corresponds in the case of a flight path of 15 m to an angular uncertainty of $\delta \Theta \approx 0.2°$ in either direction orthogonal to the beam.

As can be seen from tables 3 and 4, simulated and experimental time and position resolutions, respectively, agree quite satisfactorily for the two higher neutron energies. In case of $T_n = 181$ MeV, $\delta T_{exp}$, and $\delta Z_{exp}$ are larger than the simulated values (cf. tables 3 and 4). The reason is probably found in the number of events accumulated during the experiment; they are four times smaller than at $T_n = 417$ MeV. Hence, our $T_n = 181$ MeV data may lack statistical significance. It is concluded from the investigations of time and position resolution that both values to a large extent are determined by the intrinsic resolution of the particular photomultiplier tubes involved. It will be shown in section 4.3 that the quoted resolutions are representative for LAND.

Data discussed so far were evaluated under the conditions that the proton has hit a central region on $P_2$ of $\pm 2.5$ cm and that the neutron paddle no. 2 has fired first. Due to the geometrical arrangement, it is very likely that the first interaction of a neutron was also in paddle no. 2 in that central region which is geometrically accessible to the neutron. However, other possibilities are also conceivable. For example the neutron interacts in the central region of paddle no. 2 or further downstream (paddles no. 5, 8) without light production and light is later produced by secondary particles from the first interaction outside the geometrically accessible region of paddle no. 2. These events would, in addition, fake an increased time-of-flight. The appearance of particles moving against the neutron flight direction was already discussed in the context of fig. 1. Candidates are, indeed, observed in figs. 10 and 11, lower frame, but it is not clear whether they are due to secondary processes on a 1–2% level or whether they are remainders from C-background subtraction.

In order to further investigate the problem of backwardly moving particles, we relaxed the analysis condition. We required a proton hit on paddle $P_2$ in the central region and looked for visible energy production in neutron paddle no. 2 irrespective of the time of firing. Comparison of position spectra of paddle no. 2 under the two conditions "first hit in paddle no. 2", or "first hit elsewhere", yields an increased number of events, the relative increase is 3.2, 10.8 and 28.7% for $T_n = 181$, 417 and 662 MeV respectively. This shows the importance of backwardly scattered secondary particles at higher neutron energy. However, the position spectra are broadened only marginally from 10.6 to 11.5 cm at $T_n = 662$ MeV. This effect can be traced back to protons and $\alpha$-particles of short ranges, typically produced by evaporation from excited residual nuclei after ceasing of intranuclear cascades. Thus, such scattered particles do not significantly disturb the position measurement. Apparent neutron hits outside the geometrically accessible region are found on a 2% level in case of the condition "first hit elsewhere". They are, among others, responsible for the tail of the detector's response function, as will be discussed in the next section.

In the analysis described so far, the neutron paddle no. 2 played the central role since it is the one where kinematically allowed hits may occur. The same analysis can be carried out for the middle paddle row, i.e. for paddles no. 5, 8 and 10 which were behind paddle no. 2 (cf. fig. 8). The results of the respective analyses, which were with statistical significance only possible for the data at $T_n = 417$ MeV, are summarized in table 5. The quoted values are for FWHM as obtained from a Gaussian line fitted to the spectra. The observed deterioration of the resolution for paddles no. 5 and no. 8 followed by a slight improvement for no. 10 reflects the essential differences of detecting neutrons in the first vs consecutive paddles. The likelihood of detecting the true position of the first neutron interaction with the paddle firing first decreases the deeper the neutron penetrates. This is due to the preferred forward scattering of neutrons on heavy nuclei at higher beam energies. It is conceivable that inside the passive converters inelastic scattering or reactions deflect the neutrons from their original flight direction without producing visible energy in that paddle.

The quantities discussed at yet are not very sensitive to the correctness of the treatment of neutron interactions in the MC codes. To be specific, the only quantity used so far was the light output, or the visible energy, which was required to be larger than the threshold of 1 MeV electron equivalent energy. Additional information on the interactions of neutrons may be gained from the properties of hadronic showers developing in the neutron detector. In case of the lowest neutron energy considered, a shower may be just one proton, while at the highest energy several charged particles may be produced. As a consequence, there is some

Table 5
Time of flight and position resolution (FWHM) for cases in which a particular paddle of the central row (cf. fig. 8) fired first. The measured values contain all experimental uncertainties (see text). Data are for $T_n = 417$ MeV

| Paddle no. | $\delta T_{exp}$ [ps] | $\delta Z_{exp}$ [cm] |
|---|---|---|
| 2 | 670 | 8.3 |
| 5 | 819 | 9.2 |
| 8 | 1028 | 12.0 |
| 10 | 886 | 10.1 |

probability that visible energy is produced in more than one paddle. We call the probability distribution of the paddles which have responded to a single neutron the paddle multiplicity. This quantity is displayed in fig. 12 for neutrons with $T_n = 417$ MeV (open histogram). In this figure are also included results of HETC calculations performed for two different light output thresholds. They show some sensitivity to this quantity. Deviations from the experimental distribution may be caused by slightly different thresholds for the ten paddles used in the test experiment.

Further characteristics of the developing shower are the opening angle and the extension in neutron flight direction. Since our test array might be too small in the $X$–$Y$ plane (cf. fig. 8) to deduce properties of the full-size detector, we concentrate only on maximum shower length in $Z$-direction, i.e. perpendicular to the neutron flight direction. We required the first hit to be in paddle no. 2, its $Z$-coordinate being $Z_2$, and selected of all $Z$-coordinates of consecutively firing paddles the one for which $|Z_i - Z_2|$ has its maximum value. This is then the maximum perpendicular shower length $L_{max}^{perp}$. The distribution of $L_{max}^{perp}$ for the three neutron energies is displayed in fig. 13 together with HETC predictions. The latter contain the convolution with the position resolution of paddle no. 2 (cf. table 4) and the intrinsic paddle resolution of $\Delta Z_{int} = 5.1$ cm for paddle no. $i$. A very satisfying agreement is observed although, on a small level, indications for systematic deviations are discernible. An improvement of the code seems advisable but requires experimental data on neutron induced reactions in this energy range which are scarce (see e.g. refs. [16–18]). Nevertheless, the description of $L_{max}^{perp}$ by MC simulations is good enough to devise an algorithm for recognition of multiple hits on the basis of this and other quantities such as



Fig. 13. Distribution of the maximum shower length projected onto a plane perpendicular to the incident neutron, $L_{max}^{perp}$, for tagged neutrons of $T_n = 181$, 417 and 662 MeV. For comparison HERMES/HETC predictions are included.

average shower length, opening angle, and energy deposit.

## 3.2. Monte Carlo predictions

The response parameters of the full-size neutron detector can be estimated on the basis of computer simulations. In such an approach, the physics of the neutron induced shower as well as the detection properties of the detector elements have to be treated adequately. This is properly done by the code HERMES/HETC [10] as mentioned above.

We assume in the simulations neutrons to be emitted at time $t_0 = 0$ from a target point, which is 15 m upstream of the neutron detector. They illuminate a circle of 70 cm diameter on the detector's front area. Track is kept of each particle in the developing neutron-induced shower by recording the coordinates $X_i$, $Y_i$, $Z_i$ and time $t_i$ for all interactions $i$. The transport of light through the paddle was treated empirically on the basis of the measured effective light attenuation length (see above), and a light output threshold of 1 MeV electron equivalent energy was applied. The time of light arrival at both photomultipliers, $t_R(i)$ and $t_L(i)$, convoluted with conservative values for time resolution (a value of $\delta T = 520$ ps was used in the simulation which, in fact, is worse than that determined experi-
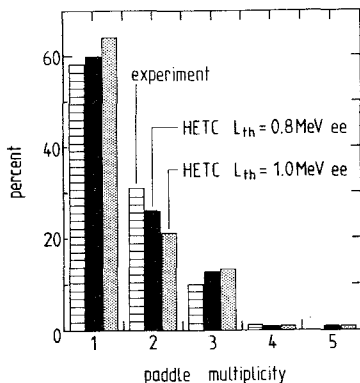


Fig. 12. Measured and simulated probability distribution of the paddle multiplicity resulting from neutrons of $T_n = 417$ MeV impinging on the ten-paddle test setup. The simulations were performed for two different light output thresholds.
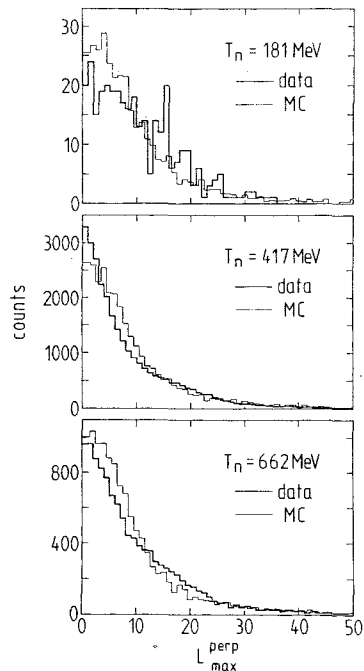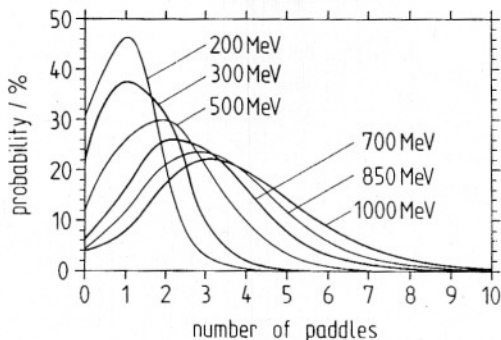
Fig. 14. Simulated probability distribution of the paddle multiplicity resulting from monoenergetic neutrons impinging on LAND with indicated energies.

broadening of the respective distribution. Both observations reflect the extending range of charged secondary particles. Depending on the neutron energy, a mean paddle multiplicity of 1–4 is observed. This number multiplied with the average multiplicity of neutrons ($\leq 5$) from a single heavy-ion interaction in the envisaged experiments has to be compared with the total number of paddles (200) in order to estimate the resolving power of the detector for multiple hits.

From the simulated values of $t_R(i)$, $t_L(i)$ one calculates either the $X$ or the $Z$ coordinate of light production depending on whether a horizontal or a vertical paddle was hit. This information is contained in the paddle number itself, which, thus, gives the complementary coordinate. (The coordinate system for the full size detector is chosen in accordance with the one defined in fig. 8) The $Y$-coordinate is always taken as the middle of the paddle which fired and, hence, has an intrinsic uncertainty of $\Delta Y = \pm 5$ cm. From the interaction position calculated in this way the one is selected at which visible energy is produced first. The corresponding time of interaction, $t^{\text{first}}$, is calculated by the mean-timing method. The "measured" position of the light production can be compared with that of the first interaction obtained from the simulation. The values $\Delta S = (\Delta X^2 + \Delta Y^2 + \Delta Z^2)^{1/2}$; which, of course, are not accessible to a measurement, are plotted in the
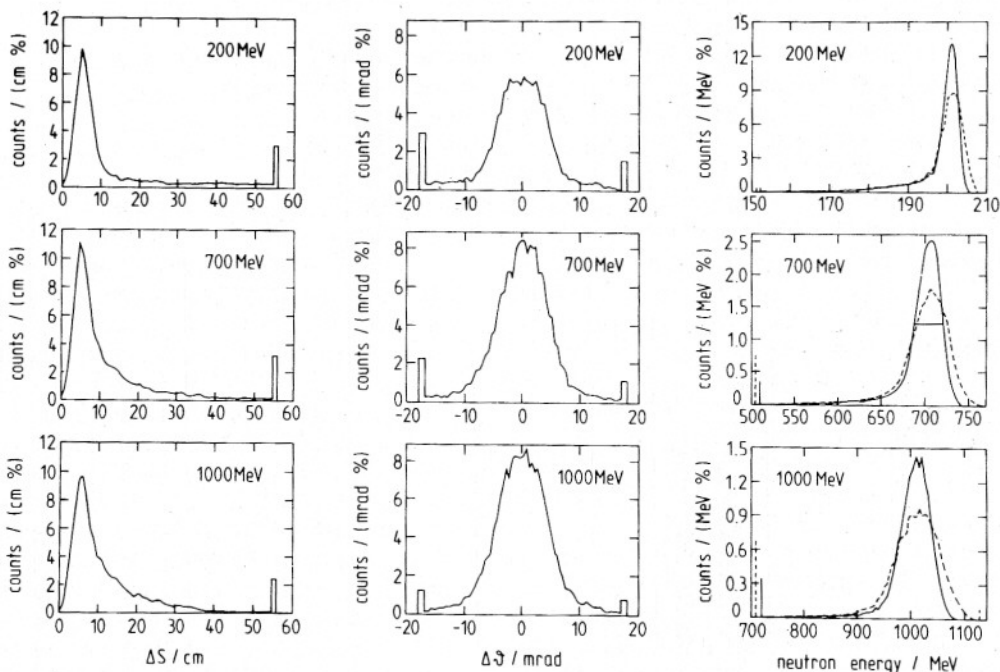
mentally), was registered as well as the number $n$ of the paddle in which visible energy was produced. These simulated data are analyzed in a second step.

The simplest analysis is to count the paddles which have fired for a single incident neutron as a function of kinetic energy (paddle multiplicity). The probability distributions obtained are reproduced in fig. 14. One observes with increasing energy both an increase of the average number of paddles which have fired, and a



Fig. 15. Simulated response function of LAND to monoenergetic neutrons of three energies. Left column: deviation, $\Delta S$, of the position of first interaction to that of the first visible energy production; middle column: change of the neutron angle due to $\Delta S$; right column: kinetic energy of neutrons as determined from time-of-flight and the measured position of first visible energy production. The results in the middle and the right frames are calculated under the assumption of a normal distance between target and LAND of $S = 15$ m while the dashed lines in the right frames refer to a distance of 10 m.

left column of fig. 15 for the three different neutron energies. A distribution in $\Delta S$ is observed which has its most probable value around $\Delta S = 5$ cm which reflects the paddle thickness of 10 cm in $Y$-direction. A tail is observed which extends, although on a small level, beyond $\Delta S = 55$ cm; those events are collected in the last bin. The position uncertainties visualized by $\Delta S$ have two consequences for LAND. First, $\Delta S$ might result in an angle uncertainty since the first interaction without detected light production has changed the scattered neutron's direction. Second, $\Delta S$ might transform into an erroneous flight path, and together with $t^{\text{first}}$ might feign an incorrect neutron kinetic energy. In the middle column of fig. 15 the observed change in flight direction is shown for three energies of incident neutrons. It is defined as $\Delta\vartheta = \vartheta_1 - \vartheta_{\text{meas}}$, where $\vartheta = $ arcsin $\{(X^2 + Y^2)/(X^2 + Y^2 + Z^2)\}^{1/2}$ is calculated either from the coordinates of the first interaction or from the "measured" ones. Of course, on the average, the direction $y$ is not altered but notable deviations $\Delta\vartheta$ are observed. As in the left column, extreme deviations ($< -17$ mrad and $> 17$ mrad) are collected in respective bins. For these evaluations, a normal distance of LAND from the target of $S = 15$ m was assumed.

For two distances $S$, neutron kinetic energies were calculated from $\Delta S$ and $t^{\text{first}}$. The results are displayed in the right column of fig. 15 for three incident energies. The solid line was calculated under the assumption $S = 15$ m, while the dashed line corresponds to a flight path of $S = 10$ m. A distribution is obtained which exceeds the incident energy, and exhibits a tail towards lower energies. The former observation is a direct consequence of the paddle thickness of 10 cm, the latter follows from large values of $\Delta S$. In summary, fig. 15 represents the response function of LAND for monochromatic neutrons.

The uncertainties are discussed with the help of fig. 16. It shows, in the upper frame, the FWHM and the standard deviation $\sigma(\Delta S)$ of the distribution of $\Delta S$ as function of neutron energy. The FWHM values increase with neutron energy since the number of paddles which fired becomes also larger (cf. fig. 14), but with increasing particle velocity, the decision which paddle fired first is less reliable, thus smearing the position of first interaction. The decrease of the standard deviation of $\Delta S$ is due to the increasing number of charged secondary particles accompanying the first interaction. They produce light for small values of $\Delta S$ immediately. Large values of $\Delta S$ are, hence, less probable at higher neutron energies (cf. fig. 15, left column), and $\sigma(\Delta S)$ decreases.

In the middle frame of fig 16, we present the FWHM and standard deviation $\sigma(\Delta\vartheta)$ of the distribution $\Delta\vartheta$ as a function of the kinetic energy of the incident neutron. The FWHM turns out to be energy
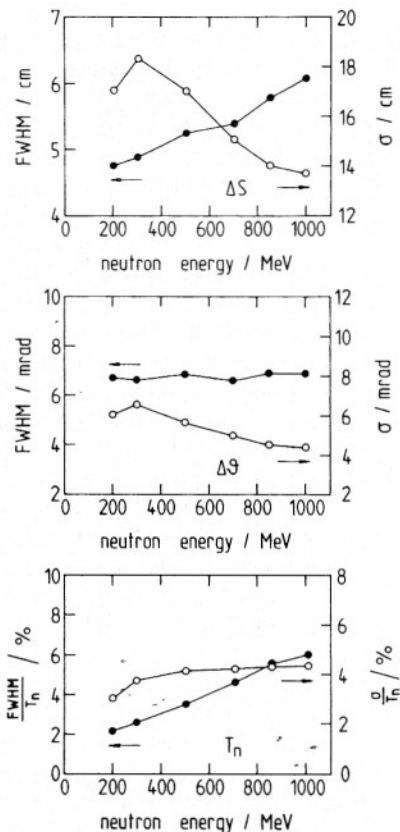


Fig. 16. Full width at half maximum (FWHM) and standard deviations of simulated response functions of LAND for various parameters as a function of neutron energy. FWHM values are indicated by full dots (left scale) while $\sigma$-values are given by open circles (right scale). Upper frame: $\Delta S$, i.e. the deviation of the position of first interaction to that of the first visible energy production; middle frame: $\Delta\vartheta$, i.e. the change of the angle of the incident neutron due to $\Delta S$; lower frame: relative kinetic energy resolution.

independent, while $\sigma(\Delta\vartheta)$ decreases, the reasons being the same as discussed for $\sigma(\Delta S)$.

The lower frame of fig. 16 contains the relative value of the FWHM and of the standard deviation $\sigma(T_n)$ of the energy response function for various neutron energies. The increase of the relative values of FWHM simply reflects the worsening of the relative time resolution $\delta T/T$ for faster particles. In the case of the variance of the relative energy resolution, this effect is partly compensated by a decreasing value of $\Delta S$, as discussed above.

This evaluation of simulated showers indicates that already the visible energy which is detected first allows for a rather accurate determination of neutron energy and position of interaction at all energies that are considered. The precision can be increased, in particular, for high neutron energies if signals from all pad-

dles responding to the developing showers are taken into account. Already the requirement of two neighbouring paddles to have fired, reduces $\sigma(T_n)/T_n$ from 4.4 to 3.5% at $T_n = 1$ GeV.

In this context, we refer back to paddle multiplicity distributions as displayed in fig. 14. It is obvious that the probability for only a single paddle to respond decreases drastically with increasing neutron energy. If, at least, two consecutive paddles were required to have fired at neutron energies of 200, 500, and 1000 MeV, then the efficiencies decrease from 70 to 23%, 90 to 65%, and 96 to 89% respectively, which is tolerable at higher neutron energies. This is, however, accompanied by a gain in resolution, since the probability for having detected the first interaction is significantly increased.

At present, we continue the MC studies with emphasis on the development of a pattern recognition algorithm which utilizes the details of the neutron induced showers (average shower length, opening angle, energy deposit, etc.) for reliable detection of multiple hits.

## 4. Operation of LAND

In this section we briefly describe the electronics and computer hardware for LAND as well as the laser system for calibration and monitoring. We also present a calibration scheme which utilizes cosmic radiation.

### 4.1. Electronics and data acquisition

The electronics is placed in the experimental area close to LAND. This is necessary in order to preserve movability of LAND within a wide angular range as required for certain experiments. As a by-product one avoids deterioration of analog pulses on long cables. Only logical or digitized signals are sent to the data acquisition system located in the control room over a distance of $\approx 20$ m. The electronics circuit is sketched in fig. 17 for the 200 LAND paddles and 40 scintillator strips of the veto detector, all of them are read out on both ends as mentioned above.

The anode pulse of each photomultiplier is split into two signals: the first one is fed via a constant fraction discriminator (CFD) into a time-to-digital converter (TDC) run in common stop mode, the second one into a charge-to-digital converter (QDC), thus yielding time and energy information, respectively. Before digitizing, timing and energy signals are delayed by 500 ns to allow for fast trigger decisions meanwhile. The energy information will be used for walk corrections of timing signals and also in the course of the analysis of shower patterns as well as for obtaining calorimetric information.
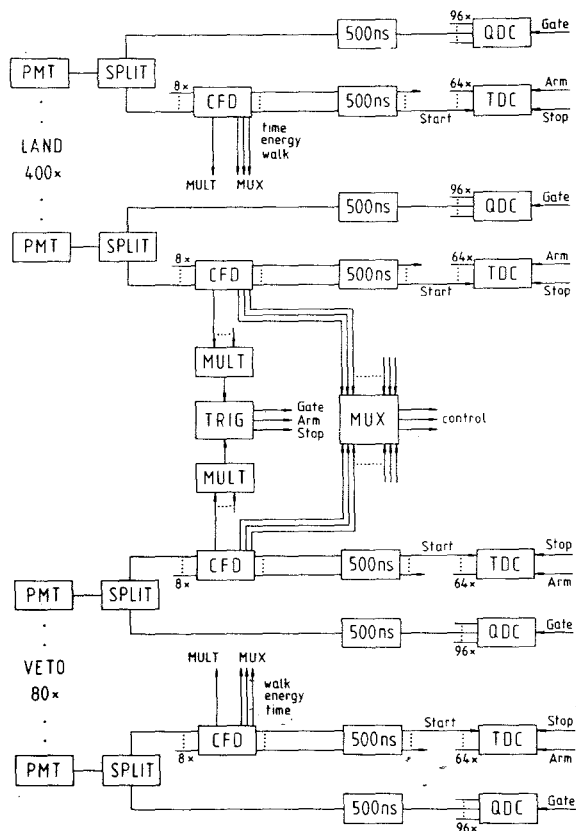


Fig. 17. Electronics used for LAND, see text for details.

All timing signals are obtained from a newly developed CFD [19]. It is a single width CAMAC module with eight inputs driving eight fast ECL outputs; in addition, a multiplicity output as well as multiplexed outputs for time, energy, and walk signals are generated. The latter signals are sent to the control room for control purposes (MUX). CFD thresholds, walk adjustments, and photomultiplier high voltages are set by remote CAMAC control. All multiplicity outputs of the CFDs serving the veto wall in front of LAND and those of LAND modules are combined into a veto multiplicity and a LAND multiplicity, respectively (MULT). These signals together with trigger information from other detectors generate a master trigger (TRIG). This trigger generates the gates on all QDCs and enables and commonly stops all TDCs.

High resolution (12 bit) QDC and TDC Fastbus [20] modules are used because of their large packing density of 96 or 64 channels, respectively, as well as their capability of being read out fast. It is possible to utilize these modules in a dual range mode (at reduced resolution) and extend thereby the dynamical range. At present, this feature is employed only for QDCs, whereas TDCs are used in a fixed range mode with a resolution of 50 ps/ch. It is possible to change the
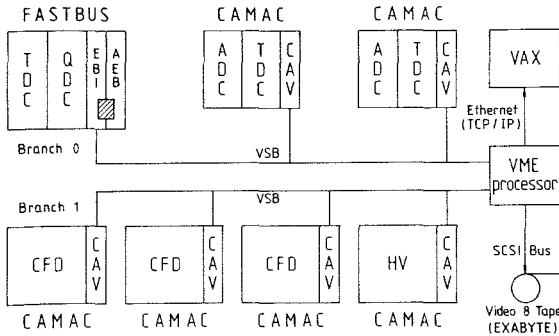
Fig. 18. Schematic setup of the data acquisition system.

resolution to 25 ps/ch for special applications. The sensitivity of all TDCs was determined with a time calibrator, that of QDCs was calibrated with cosmic radiation (see section 4.3). Relative gain factors (low/high) for TDC and QDC channels were obtained using a special calibration and trigger module.

For data acquisition the software package TDAS [21] is utilized. It is built around a VME processor, running under an OS-9 [22] operating system, which is responsible for the control of all front end electronics. It is connected via two VME subsystem busses (VSB) to Fastbus and CAMAC crates. The first branch is reserved for data acquisition (Fastbus and CAMAC) while the second one serves for controlling of CFDs and high voltage power supplies in CAMAC. Each VSB can handle up to 15 crate controllers. An overview of the data acquisition devices is depicted in fig. 18.

The Fastbus crates are read out by a dedicated processor (Aleph Event Builder/AEB) [23] which transfers the data to a dual ported memory (EBI) [24] from where they are fetched by the VME processor. Zero suppression and pedestal subtraction is done with the AEB, reducing the amount of Fastbus data by about 80%. CAMAC crates are read out directly by the VME processor with the help of a newly developed CAMAC crate controller (CAV 1000) [25]. All data are built together to one event by the VME processor. They are written to a locally attached video 8 tape in GOOSY [26] standard format.

On-line analysis and monitoring of land is done on VAX host computers in a PAW [27] environment. The communication with the VME processor takes place via ethernet using remote procedure calls [28] for control purposes and the TCP/IP transport protocol to get access to the raw data. The use of both standard FORTRAN 77 as programming language and PAW as analysis software package allows for an easy portability of all codes to a wide variety of computer types used by the collaboration at the different universities and institutes.

For a convenient handling of the parameters of all detectors a database system was developed which uses the ZEBRA package [29]. This allows access to the same database from different computers. Parameters of auxiliary detector systems can easily be added.

## 4.2. Laser system

A laser system is installed for monitoring and time calibration purposes. The principal setup is sketched in fig. 19. A central part of the laser system is a pulsed nitrogen laser VSL-337 (manufactured by Laser Science Inc., Cambridge, Mass., USA) emitting in the near UV at 337 nm. This laser contains a sealed nitrogen plasma chamber such that external gas conveyance is not needed. The power peaks at 40 kW during a 3 ns pulse with a pulse energy of about 120 μJ and an average power of ≈ 2 mW. The signal rise time is less than 200 ps. Although this laser light could be used to stimulate scintillation light in the detector paddles, we preferred, because of light attenuation problems (see below), to pump with this laser a VSL-dye laser. It contains stilbene 3 as dye, and emits deep blue laser light at 425 nm with an average power of 0.5 mW, and a pulse energy of about 20 μJ.

The laser light is sent through an electro-optical modulator consisting of an entrance Glan Taylor polarizer, a longitudinal Pockels cell, and an exit Glan Taylor polarizer (manufactured by Electro Optics Development Ltd., Basindon, Essex, UK), which is used as a variable attenuator. Through a semitransparent and a reflecting mirror the light is split into two beams which illuminate via diffusers two transport fiber bundles. The diffusers are made from opalescent glass; they broaden the laser beams without too much damping. At a distance of 20 mm behind the diffuser, a circular area is illuminated, and a Gaussian intensity distribution with a FWHM of 4 mm is observed. This
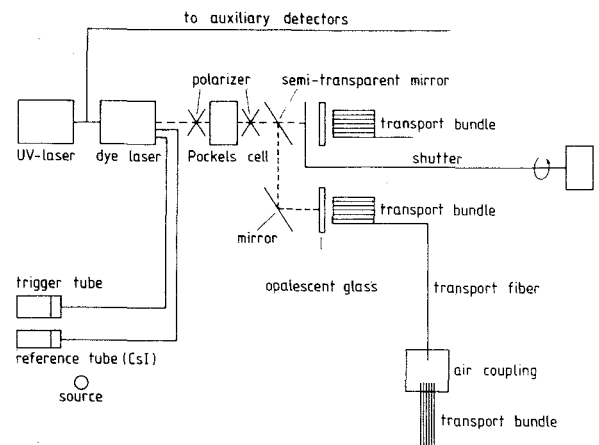


Fig. 19. Schematic setup of the laser system.

light is projected onto transport fiber bundles of 4 mm diameter which contain 37 fibers of 0.65 mm outer diameter and transport light to LAND and other detectors used in conjunction. There, each fiber of the transport bundle again illuminates over a variable distance of about 30 mm another bundle of 25 fibers that transport the light to individual detector modules, see fig. 19. Because the VSL-337 laser causes electronic noise, the system is contained in an aluminium case.

In front of the Pockels cell, two particular quartz-glass fibers are used to transport light to a so-called reference tube and to a trigger tube. The former consists of a $1 \times 1 \times 1$ cm$^3$ CsI scintillator crystal coupled to a phototube. The laser light is made incident through the detector crystal onto the photomultiplier. At the same time, the CsI scintillator is irradiated by the constant flux of 662 keV $\gamma$-rays from a $^{137}$Cs source placed close to the crystal. The event rates in the 662 keV full-energy peak and in the laser-light peak are adjusted to be approximately equal, and the pulse heights are made sufficiently different so that two completely separated peaks appear in the pulse height spectrum. The 662 keV photopeak is positioned just above the low-energy threshold of the pulse-height spectrum so that the Compton signals are discriminated. Thus, the intensity of the laser light can be normalized to the constant photopeak intensity of the $^{137}$Cs source.

The reference system was installed because the VSL laser shows two instabilities:
i) the average laser intensity decreases (by a factor of 2 after $10^7$ laser pulses) due to the finite lifetime of the nitrogen plasma chamber, and
ii) the temporal laser intensity fluctuates (by up to $\pm 5\%$) around the mean value. Already for a counting time of 4 min and a pulse frequency of 10 Hz for both the laser and the photopeak signal of the $^{137}$Cs source, the relative error in the ratio of both intensities is below 1%.

In principle, the reference tube could be used to provide the trigger for the laser-calibration signals. However, the special running conditions of the reference tube and the associated electronics necessary to process the very slow CsI signals resulted in an unacceptable time resolution. Therefore, a separate trigger tube is illuminated with laser light providing a fast trigger relative to which all times in LAND and auxiliary detectors are measured. The constant laser signal in the trigger tube in conjunction with the variable light-intensity attenuation by the Pockels cell in the LAND modules and supplementary detectors allow to determine walk effects caused by the constant-fraction discriminators.

One set of auxiliary detectors, the plastic modules of the target detector set up to determine charged-particle multiplicities [20], require calibration by UV light.

Therefore, before the UV light reaches the dye laser, part of the UV light is fed into two quartz-glass fibers that supply these modules with calibration pulses, see fig. 19.

UV light could, in principle, be coupled directly into all LAND modules. However, the total loss of intensity introduced by absorption in the fibers, by the diffuser, by the two couplings, and by the light guide turned out to be too large to render such a procedure possible. Therefore, visible dye laser light is coupled through individual fibers into the light guides of the LAND paddles. The total distance the light has to travel from the laser to the LAND paddles is made equal by carefully adjusting the fiber lengths. The two transport bundles serve light guides either on the right hand and top side or on the left hand and bottom side of LAND. A shutter blocks alternately the transport bundles; hence, LAND paddles are illuminated intermittently from two sides. This facilitates the coordination of timing signals. At present, the amount of light registered by the phototubes on LAND paddles differs significantly from tube to tube. This is mainly due to the fact that the couplings of light into the light guides of LAND paddles cannot be made identical. Hence, an energy calibration cannot be based on the laser system. Therefore, an alternative method has to be employed.

### 4.3. Calibration with cosmic radiation

Calibration of LAND can be performed using interactions of cosmic radiation which presents a natural source of signals. The hard component of the cosmic ray flux at sea level, mainly muons (97%), has sufficiently high energy (mean energy 2 GeV) to penetrate the concrete ceiling of the cave, in which LAND is installed, and to traverse the neutron detector. The total incident flux on LAND is estimated to be 600 Hz. After a sufficiently short time – short compared to the duration of production runs and long term drifts of electronics – the detector is completely scanned by cosmic rays.

In case of cosmic ray interactions we require as hardware trigger that at least five paddles have fired in coincidence in order to assure that a cosmic particle has travelled a significant way through the detector. Paddle multiplicity distributions measured with LAND peak at 12 to 13 per "cosmic event" and show maximum multiplicities of 20. They stem from events where a muon has passed the detector from side to side. These tracks can be used to calibrate LAND.

The procedure starts with a position calibration. The position of light production is calculated from the time difference of the two signals from the phototubes on each paddle. These values are accumulated into histograms. Typical position spectra exhibit a rectangular shape folded with a Gaussian-type function due to
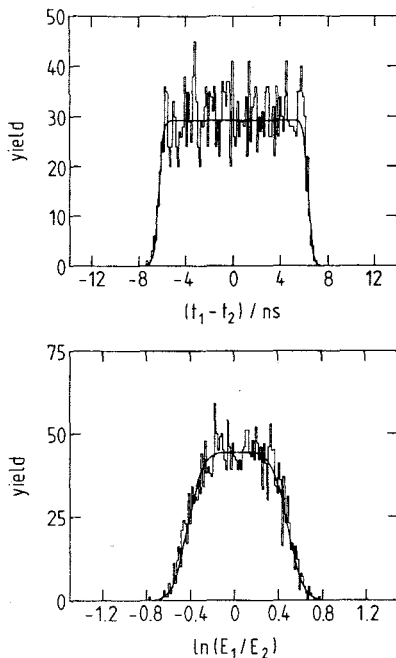
Fig. 20. Response of a LAND paddle to cosmic radiation. Upper frame: position spectrum obtained from timing signals; lower frame: position spectrum obtained from energy signals.



Fig. 21 Recorded track through LAND from a cosmic muon.

finite position resolution. An example is displayed in the upper frame of fig. 20. The width of the spectra is determined by the length of the paddle and the effective velocity of light in the scintillator. Their first moments are influenced by the difference of the time offsets in the various time circuits. They are adjusted in such a way as to center the position spectra. For the effective velocity of light we found an average value of $v_{sc} = 15.7 \pm 0.3$ cm/ns for the paddles of the neutron detector which is significantly smaller than the velocity of light in the scintillator of light in the scintillator ($c/n = 19.0$ cm/ns). The reduction is due to multiple reflections in the 0.5 cm thick plastic sheets. Once the position calibration is performed, tracks can be easily parametrized by fitting a straight line in three dimensions to the measured positions. An example of a muon track is shown in fig. 21.

Muons incident on LAND can be treated as minimum ionizing particles with velocity of light. This assumption holds for the bulk of cosmic muons even when they have passed both the concrete ceiling of the cave and LAND. A decrease of the muon velocity cannot be measured with the time resolution achievable with LAND. With these assumptions which do not apply for the small proton component of 4% in the cosmic radiation [2] one can determine the time-of-flight of a muon with respect to an arbitrarily chosen point on its track for each measured position within the neutron detector. Using this information a relative
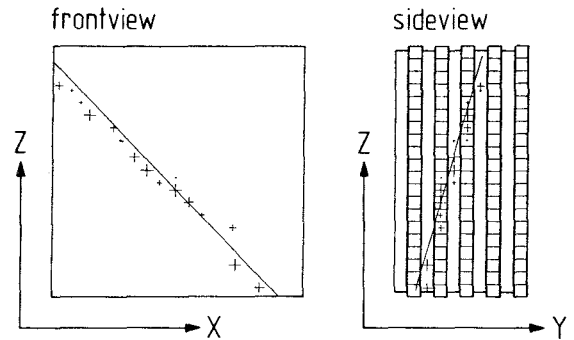
time calibration can be performed of the photomultiplier time signals. We have verified this procedure by GEANT simulations applying realistic angular, energy, and particle-species distributions for cosmic radiation [2].

From the track of a muon, which is now determined in position and time, one can calculate for each neutron detector paddle that has fired the difference between the measured quantities (time, position), and the fitted ones. The distributions of these differences reflect the resolution achievable with this method for the respective quantities. The distribution of time differences is shown in fig. 22. The FWHM values and standard deviations obtained from averaging data of $\approx 120$ paddles operational during the setup phase are $\Delta T = 600 \pm 90$ ps and $\Delta X = 8.5 \pm 3.0$ cm. These values are upper limits to the intrinsic resolution of LAND paddles since the method applied has its own inherent uncertainty which is difficult to estimate and to unfold. Also, walk effects in the CFDs were not corrected. With this reservation in mind it is fair to state that the resolutions quoted in tables 4 and 5 for a single paddle obtained with tagged neutrons is representative for LAND.
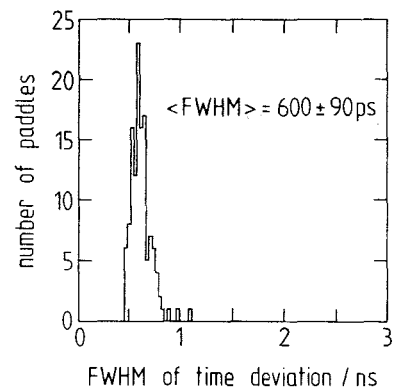


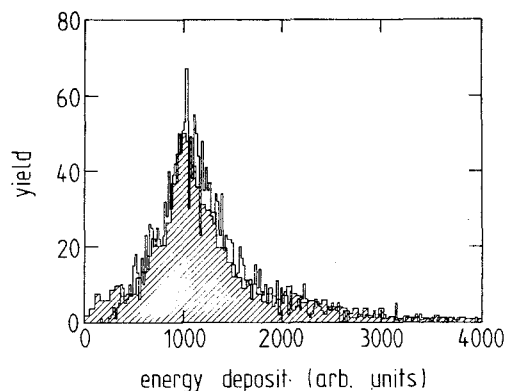Fig. 22. Distribution of time deviations (see text for definition) for $\approx 120$ paddles of LAND.

Fig. 23. Energy deposit of cosmic radiation in LAND per unit length (open histogram: experimental data; dashed area: GEANT predictions) used for absolute energy calibration.

The position of light production can also be deduced from the logarithm of the pulse height ratio of the two photomultiplier signals, $E_1$ and $E_2$ if the gains of the photomultipliers of each paddle are adjusted properly. Shifting the spectrum of $\ln(E_1/E_2)$ such that its mean is centered at zero corresponds to equalizing the gains. An example of such a position spectrum is reproduced in the lower frame of fig. 20. Obviously the resolution is not as good as in the case of position measurement via time signals (upper frame). The width of the spectrum is a measure of the absorption length $\lambda$ which was determined for $\approx 120$ paddles by this method; the results have already been presented in fig. 7.

An absolute energy calibration may also be obtained via the energy deposit $E_0$ of a muon in the paddle. It is deduced from the energy signals of the photomultiplier tubes using the relation $E_0 = 2F(E_1 E_2)^{1/2} \exp(L/2\lambda)$, where $L$ is the length of the paddle. $F$ is a correction factor which accounts for deficiencies in both light collection and absolute calibration of the gains of the photomultipliers. For cosmic tracks the path length within the paddle's plastic scintillators can be determined and the energy deposit per unit length (5 cm in the present case) can be calculated. An experimental spectrum is displayed in fig. 23 together with results of simulations where GEANT data have been subjected to the same analyses. The centroids of such distributions taken for each paddle individually correspond to the same average value of deposited energy since one deals with minimum ionizing particles. According to GEANT simulations this value is 9.3 MeV; it is used for the absolute energy calibration. The widths of such spectra are mainly due to the limited capability of the method in determining the correct path length in the plastic scintillators.

A total of about 150 000 cosmic events is necessary to obtain a reliable position, time, and energy calibration of LAND which includes determination of the effective light velocities and attenuation lengths of individual paddles. During normal production runs such an amount of data will be recorded within 80 min.

## 5. Summary

In this paper, we have presented our design studies, results of the test experiments, and Monte Carlo simulations, for a modular detector for high-energy neutrons. It features ten layers of 20 paddles, each 2 m long with a cross section of 10 cm × 10 cm, where consecutive layers are oriented orthogonal to each other. Each paddle has an alternating sandwich structure of 5 mm scintillator/5 mm passive iron converter in order to increase the detection efficiency. Light is detected by photomultipliers on either end of the paddle. The two signals are used to determine the position of light production from their difference in arrival time, while mean-timing provides, together with a start signal, the time-of-flight information. For calibration and control purpose a laser system is installed. Calibration of LAND can also be performed utilizing signals from cosmic ray interactions with LAND. The results of test experiments with tagged neutrons incident on a submodule of ten paddles showed that a momentum (energy) resolution of $\Delta p_n/p_n = 3.6\%$ ($\Delta T_n/T_n = 5.3\%$) for neutrons of $T_n = 1$ GeV for a flight path of 15 m is achievable. An angular resolution of 0.2° is observed. These experimental values can be reproduced by Monte Carlo simulations. Hence, a reliable prediction of the properties of the full detector can be given by Monte Carlo simulations. As an example we expect an efficiency of $\epsilon > 0.9$ for $T_n > 550$ MeV.

At present the detector is fully operational. A first experiment on peripheral collisions was successfully carried out [30,31].

## Acknowledgements

## References

[1] A. Gobbi and the $4\pi$-Collaboration (Darmstadt, Giessen, Heidelberg, Münster, Florence, Strasbourg, Clermont-Ferrand, Bucharest, Moscow, Zagreb), Technical Proposal of the $4\pi$ Detector for SIS/ESR, GSI-report 88-03 (1988).

[2] Particle Data Group, Review of Particle Properties, Phys. Lett. 239B (1990) 1.

[3] C.W. Fabjan, W. Struczinski, W.J. Willis, C. Kourk-oumelis, A.J. Lankford and P. Rehak, Nucl. Instr. and Meth. 141 (1977) 61.

[4] H. Abramowicz et al., Nucl. Instr. and Meth. 180 (1981) 429.

[5] T. Akesson et al., Nucl. Instr. and Meth. A241 (1985) 17.

[6] A. Andresen et al., Nucl. Instr. and Meth. A290 (1990) 95.

[7] R. Madey et al., Nucl. Instr. and Meth. 214 (1983) 401.

[8] R. Madey, W.M. Zhang, B.D. Anderson, A.R. Baldwin, B.S. Flanders, W. Pairsuwan, J. Varga, J.W. Watson and G.D. Westfall, Phys. Rev. C38 (1988) 184.

[9] R. Brun, F. Bouyant, M. Maire, A.C. McPherson, P. Zanarini (GEANT3), CERN Publication DD/EE/84-1; H. Fesefeldt (GHEISHA), Phys. Inst. TH Aachen, Report 85/02.

[10] P. Cloth, D. Filges, R.D. Neef, G. Sterzenbach, Ch. Reul, T.W. Armstrong, B.L. Colborn, B. Anders and H. Brück-mann, HERMES -- A Monte Carlo Program System for Beam–Materials Interaction Studies, Jül-2203 (Jülich, 1988).

[11] N.R. Stanton, R.M. Edelstein, J.S. Russ, R.C. Thatcher, M. Elfield, E.L. Miller, N.W. Edwards and D.R. Gill, Nucl. Instr. and Meth. 100 (1972) 355.

[12] S. Cierjacks, M.T. Swinhoe, L. Buth, S.D. Howe, F. Raupp, H. Schmitt and L. Lehmann, Nucl. Instr. and Meth. 192 (1982) 407.

[13] L.K. Rangan, E.I. Shibata and J.S. Loos, Nucl. Instr. and Meth. A276 (1989) 496.

[14] H. Folger, private communication.

[15] Y. Terrien, Neutron Beams at SATURNE, in: Neutrons at COSY, Jül-Spez.-443, 1988, eds. D. Filges and H. Freiesleben (KFA Jülich, 1988).

[16] S. Pearlstein, Summary of the Medium Energy Nuclear Data Working Group, Report BNL-NCS-40070 (1987).

[17] S. Cierjacks, Y. Hino, F. Raupp, L. Buth, D. Filges, P. Cloth and T.W. Armstrong, Phys. Rev. C36 (1987) 1976.

[18] D. Filges, P. Cloth, T.W. Armstrong, S. Cierjacks, Y. Hino, F. Raupp and L. Buth, Phys. Rev. C36 (1987) 1988.

[19] R. Albrecht, CF 8103 Octal Constant Discriminator (GSI, Darmstadt, 1989).

[20] IEEE Standard FASTBUS Modular High-Speed Data Acquisition and Control System, ANSI/IEEE Std 960-1986 (New York, 1985).

[21] Th. Blaich, R. Freifelder, N. Herrmann, J.G. Keller, P. Koczon, M. Krämer, Y. Leifels, V. Lindenstruth, W.F.J. Müller, R. Schmidt and K. Teh, GSI Scientific Report (1989) p. 311.

[22] Microware OS-9 Operating System Version 2.3, Microware Systems Corporation, Des Moines (1989).

[23] Dr. B. Struck, Technical Manual Aleph Event Builder, Tangstedt/Hamburg (1988).

[24] J. Hofmann, Dual Ported Memory EBI-VSB to FAST-BUS Interface, GSI, Darmstadt (1990).

[25] J. Hofmann, CAV 1000 CAMAC crate controller, Interface, GSI, Darmstadt (1990).

[26] H.G. Essel, H. Grein, T. Kroll, W. Kynast, W.F.J. Müller, M. Richter, H. Sohlbach, W. Spreng and K. Winkelmann, GOOSY – GSI on-line off-line system, Darmstadt (1987).

[27] R. Brun, O. Couet, C. Vandoni and P. Zanarini, PAW – Physics Analysis Workstation, CERN DD, Geneva (1989).

[28] T.J. Berners-Lee, RPC User Manual, Version 2.3.2, CERN DD/OC, Geneva (1989).

[29] R. Brun and J. Zoll, ZEBRA – Data Structure Management System, Version 3.53, CERN DD, Geneva (1987).

[30] H. Emling and the LAND collaboration, Proc. EPS-8 Meeting, Amsterdam, Netherlands 1990.

[31] H. Spies, R. Schmidt and the LAND collaboration, Proc. Int. Conf. on New Nuclear Physics with Advanced Techniques, Ierapetra, Greece, 1991.